JOURNAL OF COMPUTATIONAL PHYSICS **49**, 94–117 (1983)

Ideal MHD Stability Calculations in Axisymmetric Toroidal Coordinate Systems*

R. C. GRIMM, R. L. DEWAR, AND J. MANICKAM

Plasma Physics Laboratory, Princeton University, Princeton, New Jersey 08544

Received February 10, 1982

A scalar form of the ideal MHD energy principle is shown to provide a more accurate and efficient numerical method for determining the stability of an axisymmetric toroidal equilibrium than the usual vector form. Additional improvement is obtained by employing a class of straight magnetic field line flux coordinates which allow for an optimal choice of the poloidal angle in the minor cross section of the torus. The usefulness of these techniques is illustrated by a study (using a new code, PEST 2) of the convergence properties of the finite element Galerkin representation in tokamak and spheromak geometries, and by the accurate determination of critical β values for ballooning modes.

1. INTRODUCTION

The achievement of large β values ($\beta \equiv$ the ratio of the plasma pressure to the pressure of the externally applied magnetic field) is critical to the success of a number of toroidal plasma configurations as economically viable fusion reactors. Among the factors which can limit β in such devices, the existence of ideal MHD instabilities is one of the most fundamental. In recent years considerable progress has been made on this problem through a combination of computational and analytical studies.

Within the framework of the ideal MHD model [1], numerical methods [2–7] have proved particularly useful in studying β limitations imposed by linear instabilities in axisymmetric toroidal systems. By a careful study of the unstable eigenfunctions [8], simplified analytic theories of the most limiting internal modes (ballooning instabilities) have been developed, and these have in turn been solved by simple numerical calculations [9–11]. The combination of these computational tools has enabled detailed parameter studies of the ranges of ideal MHD stable tokamak operation [12], and together with recently developed toroidal transport codes [13–14] provides the capability of studying a wide variety of envisaged tokamak reactor schemes.

After a number of years of extensive testing, comparison, and production-running, the complex 2-D Galerkin stability packages such as PEST and ERATO have developed into robust and efficient tools and are used on a daily basis in many major

---

* Supported by U. S. Department of Energy Contract DE-AC02-76-CH03073.

0021-9991/83/010094-24$03.00/0

fusion laboratories for machine design, analysis of experimental results, and for advanced confinement studies. Nevertheless, there are computational limitations inherent in their implementation which make the application to various aspects of ideal MHD stability inaccurate, overly time consuming, or impossible. With the PEST code, for example, the choice of representation of the displacement vector prevents a study of reversed field configurations and makes a study of spheromak configurations difficult. Better representations undoubtedly exist. The original representation also contributes to pollution [15] of the MHD spectrum because the finite element expansion chosen forces incompressibility only to second order in the inverse aspect ratio. Moreover, the storage requirements of the original codes are very large, so that large toroidal mode numbers ($n \gtrsim 10$) would not be accurately treated.

For large n ballooning modes, this problem has been addressed in the finite element code ERATO by an explicit extraction of the rapidly varying ballooning phase factor from the perturbation [16]. In the Fourier representation of PEST 1 a similar result would have been effected by simply shifting the range of Fourier components in the representation. Since excellent agreement [10] at intermediate values of n can be obtained between the two-dimensional ideal MHD methods of this paper and the one-dimensional WKB ballooning mode approach, however, it seems more appropriate to treat the very short wavelength limit by the latter. This seems especially so since in this limit additional physical effects (such as finite ion-Larmor radius) become important and these can be handled in a straightforward manner in the high-n ballooning mode limit [17].

A more fundamental difficulty with these codes arises in the accurate determination of the point of marginal stability (needed to determine the critical β, for example). This has normally been done by computing the growth rate of the most unstable discrete mode for a sequence of unstable equilibria and then finding the marginal equilibrium by extrapolation to zero growth rate. A preferable computational method would involve interpolation, using values for the growth rate on both sides of $\omega^2 = 0$. Since the slow magnetosonic and shear Alfven continua can be shown analytically to appear on the stable side of the spectrum, however, it is virtually impossible to do this numerically because of the difficulty of distinguishing between discrete and continuum modes. This is especially difficult if the numerical method destabilizes the continuum [18]. The problem is further aggravated because the dependence of growth rate on β is nonanalytic at the marginal point, so that the growth rate can vary quite slowly, making extrapolation inaccurate. In this case it may even be difficult to establish definitively that stabilization occurs at any finite β.

Although these difficulties warranted attention in their own right for very accurate MHD stability analyses, the principle motivation for the work reported here is the need to extend the study of linear instabilities from ideal to resistive MHD models. Resistive instabilities may be effectively treated as a boundary layer calculation when it becomes necessary to solve the ideal MHD Euler–Lagrange equations at marginal stability in the regions between resistive boundary layers. Since the ideal MHD solutions are singular as we approach rational surfaces, it is clear that an extremely accurate numerical treatment of the ideal MHD equations is required. The development of such a method is the subject of this paper. Although there are certainly some new limitations (the absence of an estimate of the real physical growth rate is the most serious shortcoming), the method resolves most of the difficulties with the first generation stability codes mentioned above, and in most cases represents an order of magnitude improvement in the accuracy and computer time required.

This paper is arranged in the following way: In Section 2 we briefly describe the MHD equilibrium and present a class of generalized axisymmetric toroidal coordinates which can greatly improve the representation of various MHD instabilities. Section 3 is devoted to presenting a scalar form of the δW functional using a model kinetic energy normalization which can be used to study ideal MHD modes. We present the weak form of the equations (based on the Galerkin expansion method) and briefly describe the spectrum of the reduced normal mode equations. Several applications of the approach to tokamak and spheromak geometries which indicate the accuracy and efficiency of this method are given in Section 4. In Section 5 we summarize the principal conclusions of this work.

2. TOROIDAL MHD EQUILIBRIA AND FLUX COORDINATES

2.1. *Equilibrium*

We consider stationary MHD equilibria satisfying

$$\mathbf{J} \times \mathbf{B} = \nabla p, \qquad \nabla \times \mathbf{B} = \mathbf{J}, \qquad \text{and} \qquad \nabla \cdot \mathbf{B} = 0. \tag{1}$$

The most general axisymmetric toroidal equilibrium field can then be written in the form

$$\mathbf{B} = \nabla\phi \times \nabla\psi + g(\psi)\,\nabla\phi, \tag{2}$$

where $2\pi\psi$ is the poloidal flux within a magnetic surface,

$$\psi \equiv \frac{1}{(2\pi)^2} \int d\tau\, \mathbf{B} \cdot \nabla\Theta, \tag{3}$$

ϕ is the geometrical toroidal angle (Fig. 1), and Θ is an arbitrary angular coordinate varying between 0 and 2π after one complete circuit in the poloidal direction. If $p(\psi)$ and $g(\psi)$ are specified, an axisymmetric toroidal equilibrium can be determined numerically [19] by solution of the Grad–Shafranov equation

$$\Delta^*\psi \equiv X^2 \nabla \cdot (1/X^2)\,\nabla\psi = -(X^2 p' + gg'). \tag{4}$$

Here, and throughout, a prime denotes the partial derivative with respect to ψ.

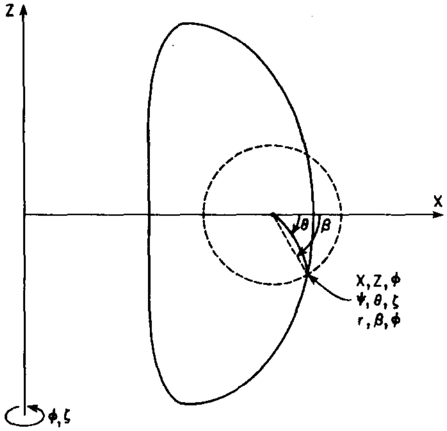

FIG. 1. Coordinate systems: cylindrical (x, z, ϕ), flux coordinates (ψ, θ, ζ), and local polar (r, β, ϕ).

2.2. *Flux Coordinate Systems*

Both analysis and computation are facilitated by an appropriate choice of coordinate system. In particular, it is essential to use a poloidal flux label as one coordinate since the mathematical form of the Euler–Lagrange equations for small perturbations is different in directions perpendicular and tangential to these surfaces. We find it convenient to use the special label ψ of Eq. (2), but it is clearly straightforward to transform to any other flux surface label by a simple one-dimensional change of variable.

Previous work has shown the advantages both numerically [4] and analytically [11] of choosing Θ and a general toroidal angle ζ so that the magnetic field lines on each magnetic surface are straight in (Θ, ζ) space. For this to hold we must have for any toroidal MHD equilibrium [20],

$$\mathbf{B} = \nabla\zeta \times \nabla\psi + q(\psi)\,\nabla\psi \times \nabla\Theta, \tag{5}$$

where q is the "safety factor." Then, from $\mathbf{J} \cdot \nabla\psi = 0$, we find

$$q\nabla \cdot (|\nabla\psi|^2\, \nabla_s \Theta) = \nabla \cdot (|\nabla\psi|^2\, \nabla_s \zeta), \tag{6}$$

where the surface operator

$$\nabla_s \equiv (\mathbf{I} - \nabla\psi\, \nabla\psi/|\nabla\psi|^2) \cdot \nabla, \tag{7}$$

with $\mathbf{I}$ being the unit dyadic. Now, since $\nabla \cdot (|\nabla\psi|^2\, \nabla_s)$ is a well-behaved elliptic partial differential operator containing no ψ derivatives, Eq. (6) determines $\Theta(\mathbf{x})$ (or $\zeta(\mathbf{x})$) (up to a function of ψ) on each magnetic surface given $\zeta(\mathbf{x})$ (or $\Theta(\mathbf{x})$). We note that

$$\mathbf{B} \cdot \nabla = \mathscr{J}^{-1}(\partial_\Theta + q\partial_\zeta), \tag{8}$$

where the Jacobian $\mathcal{J}$ is defined by

$$\mathcal{J}^{-1} \equiv \nabla\psi \times \nabla\Theta \cdot \nabla\zeta, \tag{9}$$

showing that the field lines are straight since $\zeta - q\Theta$ is constant on a field line.

Specializing to axisymmetric equilibrium configurations, we choose Θ such that

$$\nabla\Theta \cdot \nabla\phi = 0. \tag{10}$$

Then we can write more specifically

$$\nabla \cdot (|\nabla\psi|^2 \nabla_s) = \mathcal{J}_1^{-1}\partial_\Theta(\mathcal{J}_1 |\nabla\psi|^2 |\nabla_s\Theta|^2 \partial_\Theta) + |\nabla\psi|^2 |\nabla\phi|^2 \partial_\phi^2, \tag{11}$$

with

$$\mathcal{J}_1^{-1} = \nabla\psi \times \nabla\Theta \cdot \nabla\phi = |\nabla\psi|\,|\nabla_s\Theta|\,|\nabla\phi|. \tag{12}$$

Most previous numerical stability work, and specifically PEST 1, has employed the toroidal angle ϕ as one coordinate. Substituting $\zeta = \phi$ into Eq. (6), using Eqs. (10)–(12) we find

$$\partial_\Theta(X\,|\nabla\psi|\,|\nabla_s\Theta|) = 0, \tag{13}$$

or, from Eq. (12),

$$\mathcal{J}_p = X^2/\alpha(\psi), \tag{14}$$

showing that the PEST $\Theta \equiv \Theta_p$ (as defined by Eq. (14)) is the proper choice, producing straight field lines if ϕ is used as the toroidal angle. These simple PEST coordinates, however, do not necessarily result in the construction of a numerical mesh which gives optimal weighting to the regions of bad magnetic field line curvature where, for example, ballooning modes have their maximum amplitude.

More flexibility can be achieved if we use Eq. (6) to construct a generalized toroidal angle ζ after first specifying the angle Θ. To accomplish this we introduce the periodic function $\delta(\psi, \Theta)$ on each magnetic surface such that,

$$\zeta \equiv \phi - q(\psi)\,\delta(\psi, \Theta). \tag{15}$$

Note that this implies $\mathcal{J} = \mathcal{J}_1$. Equation (6) now yields

$$\partial_\Theta \delta(\psi, \Theta) = (f(\psi)\mathcal{J}/X^2) - 1, \tag{16}$$

where the surface constant

$$f(\psi) \equiv g(\psi)/q(\psi). \tag{17}$$

We note from Eq. (17) that since δ is a periodic function in Θ we must have

$$f(\psi)\langle \mathscr{J}/X^2\rangle = 1, \tag{18}$$

where $\langle\cdots\rangle$ denotes an average over Θ.

In practice, it is convenient to fix the angle Θ by specifying the Jacobian. Equation (17) then determines ζ on each magnetic surface. It is interesting to note that the PEST Θ, Θ_{p}, is simply related to any prespecified Θ through

$$\Theta_{\mathrm{p}} = \Theta + \delta(\psi, \Theta), \tag{19}$$

since

$$\mathscr{J}_{\mathrm{p}}^{-1} \equiv \nabla\psi \times \nabla\Theta_{\mathrm{p}} \cdot \nabla\phi = \nabla\psi \times \nabla\Theta \cdot \nabla\phi(1 + \delta_\Theta) = f(\psi)/X^2,$$

from Eq. (17), in agreement with Eq. (14) with $f(\psi) = \alpha(\psi)$.

The general toroidal coordinate system (ψ, Θ, ζ) constructed here is not orthogonal and its metric is more complicated than the simpler PEST coordinates since $\nabla\psi \cdot \nabla\zeta$ and $\nabla\Theta \cdot \nabla\zeta$ are not zero and $|\nabla\zeta|^2 \neq 1/X^2$. These, however, require little extra computation because of Eq. (15). The coordinate ζ is still ignorable with respect to axisymmetric equilibrium quantities, and the stability analysis can be reduced to the study of a single mode varying as exp $(in\zeta)$.

2.3. *Numerical Mapping of Equilibria*

The procedure for construction of a (ψ, Θ) mesh is essentially identical to that of mapping an equilibrium into PEST coordinates [4]. First, Eq. (4) is solved numerically for ψ. Then, we take $\mathscr{J}$ to be of the form

$$\mathscr{J}(X, Z) = X^i/\alpha(\psi)\,|\nabla\psi|^j, \tag{20}$$

where $\alpha(\psi)$ is given by the requirement that Θ increase by 2π during one poloidal circuit and we specify the integers i and j.

Equation (12) yields the basic mapping equation

$$d\Theta/ds = X/\mathscr{J}\,|\nabla\psi|, \tag{21}$$

where $ds = r^2\,|\nabla\psi|\,|\mathbf{r}\cdot\nabla\psi|^{-1}\,d\beta$ is the element of arc length along a constant ψ, ϕ line in a local polar coordinate system (r, β) centered on the magnetic axis. Thus

$$\alpha(\psi) = 2\pi\Big/\oint ds\,\frac{|\nabla\psi|^{j-1}}{X^{i-1}}, \tag{22}$$

and from Eq. (18),

$$f(\psi) = 2\pi\Big/\oint ds(X\,|\nabla\psi|)^{-1}. \tag{23}$$

Constant ψ surfaces are accurately constructed using the contouring equations

$$\partial_\beta X = (r^2/|\mathbf{r} \cdot \nabla\psi|)\, \psi_Z \tag{24}$$

and

$$\partial_\beta Z = -(r^2/|\mathbf{r} \cdot \nabla\psi|)\, \psi_X. \tag{25}$$

The quantity δ associated with the angle ζ is computed simultaneously using Eq. (16) in the form

$$\partial_\beta \delta = (f\mathcal{T}/X^2 - 1)/\partial_\beta \Theta. \tag{26}$$

Details of the computation are given in [4].

As an example, we show three different equally spaced coordinate meshes for the simple, almost constant current, analytic equilibrium [7, 21].

$$\psi = (X^2 - R^2)^2 + E^2 X^2 Z^2. \tag{27}$$

Figure 2a, with $i = 2, j = 0$ presents PEST coordinates, showing the concentration of lines of constant Θ near the corners of the D and on the small major radius side of the magnetic axis. Figure 2b shows a Hamada coordinate system with $i = j = 0$, while Fig. 2c illustrates an equal arc length system, $i = j = 1$. The latter coordinate system clearly distributes grid points more uniformly over the plasma region.

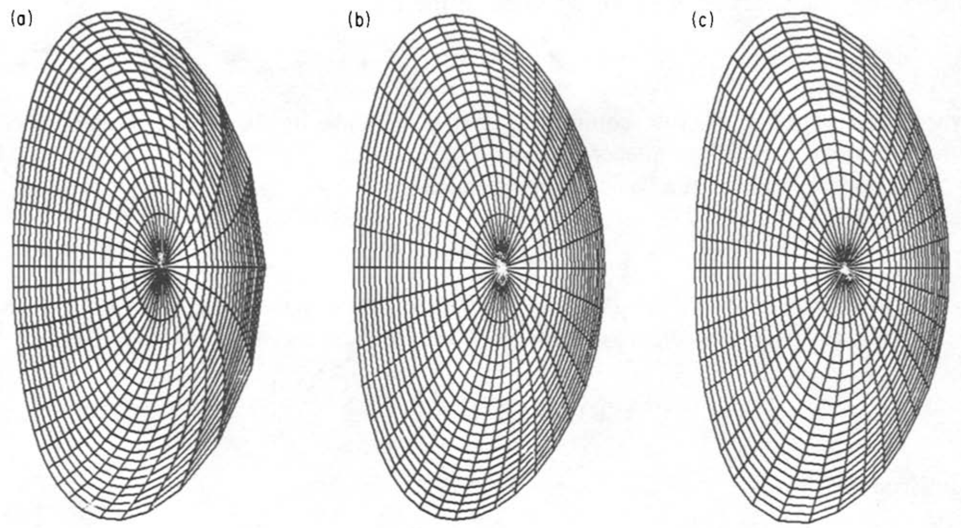

FIG. 2. Equally spaced (ψ, θ) meshes for (a) PEST, (b) Hamada, and (c) equal arc length coordinate system for the equilibrium of Eq. (27) with $R = 1$, $E = 1/2$, $q = 1.2$, $q_{\text{edge}} = 2.1$.

3. Formulation of the Stability Calculations

3.1. *Scalar Form of the Normal Mode Equations*

Solutions to the linearized ideal MHD equations can be found by extremizing the Lagrangian for small perturbations about the equilibrium state [1]. Thus we determine the Lagrangian displacement,

$$\boldsymbol{\xi}(\mathbf{x}, t) = \boldsymbol{\xi}(\mathbf{x})\, e^{i\omega t}, \tag{28}$$

for which the functional

$$L \equiv \omega^2 K(\boldsymbol{\xi}^*, \boldsymbol{\xi}) - \delta W(\boldsymbol{\xi}^*, \boldsymbol{\xi}), \tag{29}$$

is stationary. Here the kinetic energy functional

$$2K(\boldsymbol{\xi}^*, \boldsymbol{\xi}) = \int_p \rho\, |\boldsymbol{\xi}|^2\, d\tau, \tag{30}$$

and the change in potential energy,

$$2\delta W(\boldsymbol{\xi}^*, \boldsymbol{\xi}) \equiv \int_p d\tau [|\mathbf{Q} + (\boldsymbol{\xi} \cdot \nabla\psi)\mathbf{J} \times \nabla\psi/|\nabla\psi|^2\,|^2 + \gamma p\, |\nabla \cdot \boldsymbol{\xi}|^2 - 2U\, |\boldsymbol{\xi} \cdot \nabla\psi|^2]$$

$$+ \int_v d\tau\, |\nabla \times \mathbf{A}|^2. \tag{31}$$

Here $\mathbf{Q} \equiv \nabla \times (\boldsymbol{\xi} \times \mathbf{B})$, $\mathbf{A}$ is the vector potential for the perturbed magnetic field in the vacuum and

$$2U = 2p'\kappa_\psi + \sigma^2 B^2/|\nabla\psi|^2 - \mathbf{B} \cdot \nabla[\sigma(\mathbf{s} \cdot \nabla\psi)/|\nabla\psi|^2] + \sigma q'/\mathscr{J}. \tag{32}$$

In the last expression we have defined

$$\mathbf{s} \equiv \nabla\zeta - q\, \nabla\Theta, \tag{33}$$

$$\sigma \equiv \mathbf{J} \cdot \mathbf{B}/B^2 = -g' - gp'/B^2, \tag{34}$$

and the field line curvature

$$\boldsymbol{\kappa} \equiv \mathbf{B}/B \cdot \nabla(\mathbf{B}/B) = \kappa_\psi \nabla\psi + \kappa_s \mathbf{s}, \tag{35}$$

with

$$\kappa_\psi = p'/B^2 + \partial_\psi(B^2)/2B^2 + [\nabla\psi \cdot \nabla\Theta/X^2 - g(q\delta)'/\mathscr{J}]\, \partial_\Theta(B^2)/2B^4. \tag{36}$$

Following previous work, we decompose the displacement vector as

$$\boldsymbol{\xi} = \xi^\psi \mathbf{B} \times \mathbf{s}/B^2 + i\xi^s \mathbf{B} \times \nabla\psi/B^2 + i\xi^b \mathbf{s} \times \nabla\psi/B^2, \tag{37}$$

noting that $\mathbf{B} = \mathbf{s} \times \nabla\psi$.

In general, the normal mode equations which result from carrying out the extremization of Eq. (29) involve each of the three components of $\boldsymbol{\xi}$. Although special consideration was taken in previous work to project $\boldsymbol{\xi}$ into polarizations which effect a partial diagonalization of δW, the eigenfunction corresponding to a typical unstable normal mode will contain contributions from all three components which must be computed in order to obtain a physically meaningful growth rate. If, however, as is often the case, we are interested primarily in the accurate determination of marginal stability and not in the exact growth rates and eigenfunctions, considerable simplification of Eq. (29) is possible by analytically minimizing δW wth respect to ξ^s and ξ^b, thus eliminating them from the functional. This exercise was first carried out by Bineau [22].

Instead of the complete kinetic energy normalization of Eq. (30), we therefore employ the model normalization

$$2K(\xi^*, \boldsymbol{\xi}) = \int_p d\tau\, \boldsymbol{\xi}^* \cdot \underline{\underline{\rho}} \cdot \boldsymbol{\xi} \tag{38}$$

with anisotropic density, $\underline{\underline{\rho}} = \rho\, \nabla\psi\, \nabla\psi$, so that inertia affects displacements only in the direction normal to a magnetic surface. Displacements within a surface, however, still minimize δW, even at finite growth rate. Such a nonphysical density profoundly modifies the nature of the continuous spectrum (see Section 3.2), but leaves unchanged the number of unstable discrete modes. As shown in the Appendix, Eq. (31) can be reduced to

$$\begin{aligned} 2\delta W(\xi^*, \xi) = \int_p d\tau\, [&-\mathscr{J}^{-1}(P\xi)^* \Delta_s^{-1} \mathscr{J}^{-1} P\xi + |\mathbf{B} \cdot \nabla\xi|^2/|\nabla\psi|^2 \\ &+ \gamma p(|\langle \mathscr{J}\xi\rangle'|^2/\langle \mathscr{J}\rangle^2) - 2U|\xi|^2 + 2\delta W'_{\text{ind}}\,\delta_{n,0}] + \int_v d\tau\, |\nabla \times \mathbf{A}|^2, \end{aligned} \tag{39}$$

where

$$P\xi \equiv \mathscr{J}\nabla \cdot [(\mathbf{B} \cdot \nabla\xi\, \nabla\psi - \mathbf{J} \times \nabla\psi\, \xi)/|\nabla\psi|^2], \tag{40}$$

$$\Delta_s \equiv \nabla \cdot \nabla_s, \tag{41}$$

and unambiguously, $\xi \equiv \boldsymbol{\xi} \cdot \nabla\psi = \xi^\psi$, since it is well known that the change in potential energy in the vacuum can be reduced to a quadratic form involving only ξ on the plasma–vacuum surface. The last term in the first expression of the right-hand side in Eq. (39), given explicitly below in Eq. (45), contributes only to axisymmetric perturbations ($n = 0$) and represents an internal "inductive" stabilization which arises because an axisymmetric compressible Lagrangian displacement causes additional perturbed current fluxes.

In terms of the general (ψ, Θ, ζ) coordinate system of the last section, explicit forms for the quantities in Eqs. (39)–(41) are

$$\begin{aligned} 2U = {} & -p'(X^2)'/X^2 - (X^2p' + gg')(\mathscr{J}/X^2)'/\mathscr{J} + (X^2p' + gg')^2/(X^2\,|\nabla\psi|^2) \\ & - \mathscr{J}^{-1}\partial_\Theta[\mathscr{J}(X^2p' + gg')\,\nabla\psi\cdot\nabla\Theta/(X^2\,|\nabla\psi|^2)], \end{aligned} \tag{42}$$

$$\begin{aligned} P\xi = {} & (\partial_\Theta + q\partial_\zeta)\xi' + q'\partial_\zeta\xi + \partial_\Theta\{\nabla\psi\cdot\nabla\Theta[(\partial_\Theta + q\partial_\zeta)\xi]/|\nabla\psi|^2 \\ & + (X^2p' + gg')\xi/|\nabla\psi|^2\} \\ & - \partial_\zeta\{[(q\delta)' + q\delta_\Theta\nabla\psi\cdot\nabla\Theta/|\nabla\psi|^2](\partial_\Theta + q\partial_\zeta)\xi \\ & + [g'\mathscr{J}/X^2 + q\delta_\Theta(X^2p' + gg')/|\nabla\psi|^2]\xi\}, \end{aligned} \tag{43}$$

$$\begin{aligned} \mathscr{J}\Delta_{\rm s} = {} & \partial_\Theta(X^2/\mathscr{J}\,|\nabla\psi|^2)\,\partial_\Theta + \partial_\zeta(\mathscr{J}/X^2 + q^2X^2\delta_\Theta^2/\mathscr{J}\,|\nabla\psi|^2)\,\partial_\zeta \\ & - \partial_\Theta(qX^2\delta_\Theta/\mathscr{J}\,|\nabla\psi|^2)\,\partial_\zeta - \partial_\zeta(qX^2\delta_\Theta/\mathscr{J}\,|\nabla\psi|^2)\,\partial_\Theta, \end{aligned} \tag{44}$$

and

$$\begin{aligned} 2\langle\mathscr{J}\rangle\,\delta W'_{\rm ind} = {} & g^2\,|\langle\mathscr{J}\xi/X^2\rangle'|^2/\langle\mathscr{J}/X^2\rangle + |\langle\mathscr{J}\,|\nabla\psi|^2\,\xi'/X^2\rangle + \langle\mathscr{J}\nabla\psi\cdot\nabla\theta(\partial_\theta\xi)/X^2\rangle \\ & + \langle\mathscr{J}(gg' + X^2p')\xi/X^2\rangle|^2/\langle\mathscr{J}\,|\nabla\psi|^2/X^2\rangle. \end{aligned} \tag{45}$$

In obtaining these expressions, it is useful to note the flux coordinate form of Eq. (4),

$$\partial_\psi(\mathscr{J}\,|\nabla\psi|^2/X^2) + \partial_\Theta(\mathscr{J}\,\nabla\psi\cdot\nabla\Theta/X^2) = -\mathscr{J}(X^2p' + gg')/X^2. \tag{46}$$

The problem of determining the instability of a toroidal equilibrium is then equivalent to demonstrating the existence of solutions ξ, normalized according to Eq. (38), which make Eq. (39) negative. This is obvious since the energy principle attaches significance only to the sign of δW—the point of marginal stability is not affected by the change in normalization. Clearly the eigenvalues and eigenfunctions of the normal mode equations corresponding to this reduced problem are not equivalent to those found by extremizing Eq. (29). But the point of marginal stability is the same, and for many applications, expecially when the unstable eigenfunction is a slowly varying function of ψ, the behavior of $\boldsymbol{\xi}\cdot\nabla\psi$ obtained from the reduced problem is qualitatively very similar to that obtained with the full normalization.

3.2. *Spectrum of the Reduced Normal Mode Equations*

The spectrum of perturbations $\boldsymbol{\xi}$ which extremize Eq. (39) with Eq. (38) is considerably different from the usual ideal MHD spectrum [23, 24]. Physically, the model kinetic energy normalization has restricted the nonaxisymmetric perturbations to incompressible modes, thereby removing the slow magnetosonic continuum branch, while the subsequent elimination of $\mathbf{B}\times\nabla\psi\cdot\boldsymbol{\xi}$ has eliminated the fast magnetosonic stable discrete part of the spectrum. The set of solutions remaining include both discrete modes and a continuum corresponding to the usual shear Alfven spectrum, but displaced "upwards" so that there is a gap between the marginal point $\omega^2 = 0$ and the lowest value of ω^2 in the continuum (assuming Mercier stability).

Information about the nature of the reduced normal modes can be obtained by examining their asymptotic behavior near the singular surfaces of the corresponding

Euler–Lagrange equations. These occur on the equilibrium magnetic surfaces ($\psi = \psi_s$) where $\mathbf{B} \cdot \nabla\xi$ approximately vanishes, i.e., surfaces for which the safety factor q is rational (l/n). In addition to the class of square integrable regular solutions, we find asymptotically singular solutions of the form

$$\xi \sim x_{\pm}^{p_{\pm}} \exp i(l\Theta - n\zeta), \tag{47}$$

where $x \equiv \psi - \psi_s$ and

$$p_{\pm} = -\tfrac{1}{2} \pm (-D_I - \Gamma\omega^2)^{1/2}. \tag{48}$$

Here D_I, the usual measure of localized ideal MHD interchange stability [20, 25] (Mercier's criterion), is taken to be negative and

$$\Gamma \equiv (p'/q'^2)\langle \mathscr{J} B^2/|\nabla\psi|^2 \rangle \langle \mathscr{J} \rangle. \tag{49}$$

There are four such solutions in the vicinity of each rational surface—one for each value of p and one for each of the generalized functions [26],

$$\begin{aligned} x_{\pm}^{p} &\equiv |x|^{p}, && \text{if} \quad x \gtrless 0, \\ &\equiv 0, && \text{if} \quad x \lessgtr 0. \end{aligned} \tag{50}$$

Away from marginal stability ($\omega^2 = 0$) we discard the most negative root for p since it does not satisfy the finite model kinetic energy normalization

$$\int_p d\tau\, \rho\, |\xi|^2 < \infty. \tag{51}$$

The inclusion of these "big" singular solutions is, however, essential to a proper treatment of the ideal MHD solutions at marginal stability required in a boundary layer treatment of resistive modes. This will be the subject of future work.

From Eq. (48) we see that the continuum reaches down to the point $\omega_c^2 = |D_I|/\Gamma > 0$, giving the possibility of avoiding the numerical difficulties associated with accurately predicting marginal stability criteria as discussed earlier in this paper. When $\omega^2 < (|D_I| - \frac{1}{4})/\Gamma$, the small singular solution vanishes asymptotically in the vicinity of the singular surface and a weak solution can be represented [27] by a Galerkin expansion in terms of functions belonging to the space $\mathscr{H}^1$. Otherwise, for $(|D_I| - \frac{1}{4})/\Gamma < \omega^2 < |D_I|/\Gamma$, there will be a weak singularity (ξ is square integrable, but ξ' is not) for unstable modes near the marginal point (e.g., the internal $m = 1$ kink mode) for which special attention is required. The proper representation of these modes are also to be reported on elsewhere [28].

3.3. *Galerkin Representation of the Reduced Normal Mode Equations*

[redacted]

$$\xi(\psi, \Theta, \zeta) = \sum_{l=-|L|}^{|L|} \sum_{m=1}^{M} \xi_{lm} u_m(\psi)\, e^{i(l\Theta - n\zeta)} \tag{52}$$

into Eqs. (38) and (39). The weak form of the normal mode equations can then be written as the generalized eigenvalue problem,

$$W_{l'lm'm}\xi_{lm} = \omega^2 K_{l'lm'm}\xi_{lm} \tag{53}$$

with

$$2W_{l'lm'm} = (2\pi)^2 \int_0^{\psi_a} d\psi\, [u_{m'} \quad u'_{m'}] \begin{bmatrix} W_{l'l} & Y^{+}_{l'l} \\ Y_{l'l} & Z_{l'l} \end{bmatrix} \begin{bmatrix} u_m \\ u'_m \end{bmatrix} + V_{l'lm'm}\delta_{m'M'}\delta_{mM} \tag{54}$$

and

$$2K_{l'lm'm} = (2\pi)^2 \int_0^{\psi_a} d\psi\, u_{m'}\, \rho S_{l'l} u_m. \tag{55}$$

Here

$$W_{l'l}(\psi) = \sum_{k,k'} Q^{+}_{l'k'} G_{k'k} Q_{kl} + (l' - nq)(l - nq)\, J_{l'l} + M_{l'l} + W^{0}_{l'l}\delta_{n0},$$

$$Y_{l'l}(\psi) = \sum_{k} (l' - nq)\, G_{l'k} Q_{kl} + Y^{0}_{l'l}\delta_{n0},$$

$$Z_{l'l}(\psi) = (l' - nq)(l - nq)\, G_{l'l} + Z^{0}_{l'l}\delta_{n0},$$

with

$$G^{-1}_{l'l} = n^2 E_{l'l} + nq(l' + l)\, V_{l'l} + l'lF_{l'l},$$

$$Q_{l'l} = l'(l - nq)\, A_{l'l} + n(l - nq)\, D_{l'l} + l'B_{l'l} + nqU_{l'l} + ng'C_{l'l}/f$$
$$+ nqf'\delta_{l'l}/f,$$

and

$$\begin{aligned} A_{l'l} &= \langle l' |\, i\, \nabla\psi \cdot \nabla\Theta/|\nabla\psi|^2\, | l \rangle, \\ B_{l'l} &= \langle l' |\, (gg' + X^2 p')/|\nabla\psi|^2\, | l \rangle, \\ C_{l'l} &= \langle l' |\, \delta_\Theta\, | l \rangle, \\ D_{l'l} &= \langle l' |\, i[(q\delta') + q\, \nabla\psi \cdot \nabla\Theta\, \delta_\Theta/|\nabla\psi|^2]\, | l \rangle, \\ U_{l'l} &= \langle l' |\, (gg' + X^2 p')\delta_\Theta/|\nabla\psi|^2\, | l \rangle, \\ E_{l'l} &= \langle l' |\, \mathscr{I}/X^2 + q^2 X^2 \delta_\Theta^2/(\mathscr{I}\, |\nabla\psi|^2)\, | l \rangle, \end{aligned} \tag{56}$$

$$V_{l'l} = \langle l' | X^2 \delta_\Theta / (\mathscr{J} |\nabla\psi|^2) | l \rangle,$$

$$F_{l'l} = \langle l' | X^2 / (\mathscr{J} |\nabla\psi|^2) | l \rangle,$$

$$J_{l'l} = \langle l' | 1 / (\mathscr{J} |\nabla\psi|^2) | l \rangle,$$

$$\begin{aligned} M_{l'l} = \langle l' | \, & [\mathscr{J} p' (X^2)'/X^2 + (X^2 p' + gg')(\mathscr{J}/X^2)' \\ & + i(l' - l)\mathscr{J}(X^2 p' + gg') \nabla\psi \cdot \nabla\Theta / (X^2 |\nabla\psi|^2) \\ & - \mathscr{J}(X^2 p' + gg')^2 / (X^2 |\nabla\psi|^2)] \, | l \rangle, \end{aligned}$$

$$R_{l'l} = \langle l' | \mathscr{J}' | l \rangle,$$

and

$$S_{l'l} = \langle l' | \mathscr{J} | l \rangle.$$

The terms $W^0_{l'l}$, $Y^0_{l'l}$, and $Z^0_{l'l}$ which must be added for axisymmetric perturbations are given in the Appendix, $\delta_{l',l}$ is the usual Kronecker symbol, and δ_Θ is given by Eq. (16). The bracket notation is used to represent Fourier matrix elements, for example,

$$G^{-1}_{l'l} \equiv -\langle l' | \mathscr{J} \Delta_s | l \rangle = -\frac{1}{2\pi} \oint e^{-il'\Theta} \mathscr{J} \Delta_s e^{il\Theta} \, d\Theta. \tag{57}$$

The procedure for constructing the matrix elements of Eq. (54) is straightforward and essentially follows [4]. We select a set of piecewise linear finite elements for the $u_m(\psi)$, $m = 1, M$ and truncate the Fourier expansion at $|l| \leqslant |L|$. Typically, $M \lesssim 50$, $L \lesssim 20$. We construct and invert **G**, the Fourrier representation of the operator $-\mathscr{J}\Delta_s$ of Eq. (41), on each of an arbitrarily spaced set of magnetic surfaces used to represent the finite element radial expansion functions $u_m(\psi)$. Then **G** is found by matrix inversion. We can then compute the matrices **W**, **Y**, and **Z** on each surface and perform the integrations over ψ in Eqs. (54) and (55) by numerical quadratures. The eigenvalues of the generalized matrix problem of Eq. (53) are found by inverse iteration [29]. The representation of the perturbed vacuum potential energy $V_{l'lM'M}$ is essentially identical to that of [4]; the expressions in that work being modified only by a simple similarity transformation, $T_{l'l} = \langle l' | e^{inq\delta} | l \rangle$, arising from the generalization of the ignorable toroidal angle ζ. Naturally, $T_{l'l} = \delta_{l',l}$ in PEST coordinates.

4. Numerical Results

The PEST 2 stability code, embodying the formulation of the last two sections, has developed through several stages. Beginning with PEST 1, the first version was restricted to PEST coordinates (Eq. (14)) and checked extensively against PEST 1. The considerable improvement in execution time and reduction in memory requirements led to extensive application (on the CRAY–1) to the study of large n ($\sim$20) ballooning modes [11] and to the development of a special version of the code which can be usefully employed on a small computer (DEC KI–10). These early versions have now been rewritten to accept equilibrium quantities from an arbitrarily spaced radial mesh and to provide the option of rezoning this mesh to allow various nodes of the radial finite elements to coincide with the rational surfaces. In this section we present a variety of test calculations which demonstrate the accuracy and usefulness of the PEST 2 approach.

4.1. *Comparison with* PEST 1

A direct comparison of growth rates from PEST 1 and PEST 2 is not possible because of the choice of different normalizations in Eqs. (30) and (38), respectively. It is, of course, still possible to check the signature of δW and this is reported in the next section. Here we present a set of comparison calculations performed after modifying the PEST 1 code to adopt the model normalization of Eq. (38).

We consider the analytic, almost constant current, toroidal equilibrium of Eq. (27), which has been used previously for extensive comparison of stability codes [7]. For the equilibrium of Fig. 2, we illustrate in Table I the convergence versus L, (where we include all Fourier components (l) in the range $-L \leqslant l \leqslant L$), for PEST 1 (modified) in column 1, for PEST 2 using PEST 1 coordinates in column 2, and for PEST 2 using an equally spaced mesh in $\Psi/2\pi$ and PEST(θ_{p}), Hamada(θ_{H}), and equal arc length (Θ_{E}) meshes in columns 3, 4, and 5, respectively. We have chosen to study an $n = 1$ external kink with a vacuum of infinite extent surrounding the plasma column because it emphasises the differences between the various calculations compared with an internal mode. The data presented for each value of L were obtained after extrapolating to infinity in the number of radial finite elements (using $M = 24$, 36, and 48). For all cases the equilibrium mesh employed 128 equally spaced θ grid points and the matrix $G_{l'l}$ of Eq. (57) in PEST 2 was evaluated with $-25 \leqslant l, l' \leqslant 25$.

Columns 1 and 2 represent stability calculations carried out with mapped equilibrium data located on identical meshes. The differences are due principally to the different representations of $\boldsymbol{\xi}$, the exact vanishing of $\nabla \cdot \boldsymbol{\xi}$ in PEST 2, and to the surface by surface elimination $\mathbf{B} \times \nabla\psi \cdot \boldsymbol{\xi}$ using $\mathbf{G}^{-1}$ of Eq. (57), rather than the global elimination which occurs in PEST 1 with the normalization of Eq. (30). The more rapid convergence in PEST 2 reflects this improvement in the representation.

TABLE I

		PEST 2			
L	PEST 1M	$\psi_{\mathrm{p}}, \Theta_{\mathrm{p}}$	Θ_{p}	Θ_{H}	Θ_{E}
5	−7.5046	−9.1110	−9.0441	−9.4853	−9.9381
10	−9.3435	−9.4137	−9.4152	−9.4113	−9.4254
12	−9.3807	−9.4135	−9.4160	−9.4113	−9.4125
15	−9.3855	−9.4135	−9.4162	−9.4113	−9.4091

We note that halving the required number of Fourier components to get a reliable answer (which appears to be typical) results in the necessity of storing $(3 \times 2)^2 = 36$ times fewer matrix elements since PEST 2 determines only one component of $\boldsymbol{\xi}$. The reduction in computer time is also significant since, although additional effort must be performed to invert $\mathbf{G}$ in PEST 2, this is usually small compared to the reduction in the total number of matrix elements to be computed and to the consequent reduction in the time required to determine the eigenvalues [7] ($\sim L^2$).

The differences between columns 2 and 3 reflect the dependence of PEST 2 on the ψ coordinate mesh. An equally spaced PEST 1 ψ ($\propto \int d\tau/X^2$) coordinate mesh (in column 2) concentrates the finite-element representation nearer the plasma–vacuum interface than the $\psi \equiv \Psi/2\pi$ system of column 3. Since the external modes have their maximum amplitude near the plasma surface, it is not surprising that column 2 gives a more unstable result with small l. Internal modes, where the destabilizing terms are localized closer to the magnetic axis, are on the other hand better represented by the PEST 2 ψ mesh. In general, an accurate estimate of the growth rate in either case requires extrapolation to the limit in the number of radial finite elements as described in previous work.

The final columns of Table I give a comparison of the convergence rates for these different Θ meshes. For this medium aspect ratio, low-β equilibrium, it is seen that the convergence in each case is quite rapid with the equal arc length θ being slightly slower. Figure 2 indicates that both θ_{p} and θ_{H} coordinates give an improved resolution near the top/bottom of the D. We also note that, in this case, the direction of convergence is from the unstable side with both Hamada and equal arc length coordinates. This can occur computationally because discretization errors in the representation of the operator Δ_{s}^{-1} can violate the variational character of the minimization of δW. In this case, however, where the errors in Δ_{s}^{-1} are very small, the dominant cause for the absence of a lower bound is not related to this effect, but occurs because our treatment of δW in the vacuum region is not variational [4].

We have mentioned that the choice of normalization followed here (Eq. (38)) results in nonphysical eigenfunctions when $\omega^2 \neq 0$. Although the numerical solution of Eq. (53) determines only the component $\boldsymbol{\xi} \cdot \nabla\psi$, the other components can then easily be compued by direct substitution into the $\mathbf{B} \times \nabla\psi$ and $\mathbf{B}$ components of the Euler–Lagrange equations using Eqs. (A4) and (A9). We illustrate the behavior of the eigenfunction in Fig. 3, comparing it with the eigenfunction using the complete kinetic energy normalization computed from PEST 1. Plotted here are vectors representing the component of $\boldsymbol{\xi}$ in the poloidal plane. The enhancement of the perturbation near the plasma surface in Fig. 3b comes partially from the presence of the $q = 2$ surface which lies near the plasma–vacuum interface ($q_a = 2.4$) and indicates that the $\mathbf{B} \times \nabla\psi \cdot \boldsymbol{\xi}$ and $\mathbf{B} \cdot \boldsymbol{\xi}$ components vary more rapidly than $\boldsymbol{\xi} \cdot \nabla\psi$ in those regions.

4.2. *Calculation of Critical Parameters Corresponding to Marginal Stability*

We have described how the approach of this work allows an accurate calculation of the point of marginal stability because it is possible to follow the unstable mode

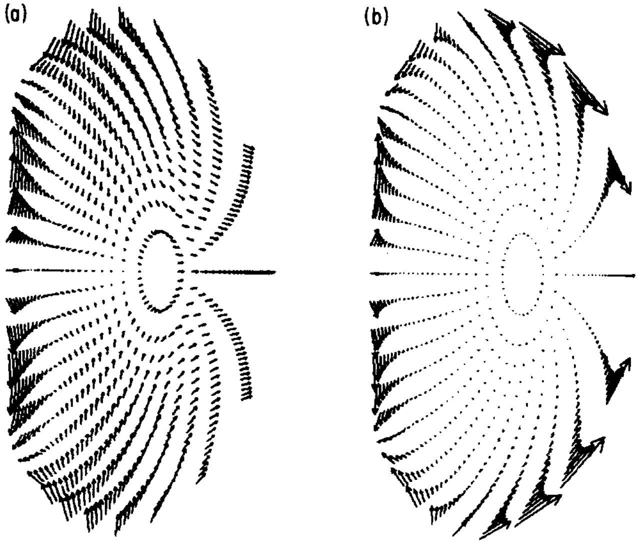

FIG. 3. Eigenfunction for the predominantly $m = 3$, $n = 1$ surface kink mode for the equilibrium of Fig. 2; (a) with complete kinetic energy normalization, Eq. (30); (b) with model normalization, Eq. (38).

across the marginal point. In Fig. 4 we illustrate this point for a sequence of flux-conserving equilibria with pressure and safety factor profiles fitted to a set of data taken from the PLT experiment. In the notation of [12], the equilibria are circular ($R/a = 3.3$) with $p(\psi) = p_0(1-\psi)^{5.1}$ and $q(\psi) = 1.16(1-0.04125\psi)^{-2.19}$. The equilibria were computed with the equilibrium code described in [19] using a rectangular 65×65 mesh.

The stability of the sequence to the $n = 3$ internal ballooning mode was studied using both PEST 1 (open circles) and PEST 2 (crosses). The PEST 2 calculations were made with the PEST Θ-coordinate, and all data shown have been extrapolated

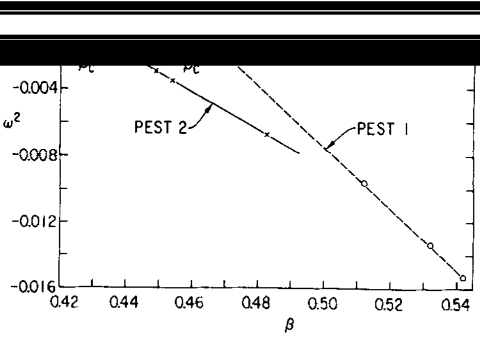

FIG. 4. Estimation of critical β values (in %) (O) from PEST 1 and (X) from PEST 2. With PEST 2 the ability to interpolate using values in the stable side of $\omega^2 = 0$ improves the estimate.

to the limit in both the number of radial finite elements and in the number of Fourier modes in the Θ direction.

Since the numerical value of the growth rate obtained with PEST 2 is in arbitrary units, we have normalized the values from PEST 2 to those of PEST 1 by multiplying each by the factor $\omega_1^2(\beta=0.51)/\omega_2^2(\beta=0.51)$. For actual comparison with Fig. 4, $\omega_2^2(\beta=0.51)=-0.412$.

A direct comparison of this type provides a useful check on the accuracy of previous calculations made with PEST 1. Although versions with greater resolution have been constructed for studies of the internal kink and for tilting modes in spheromaks, the version used here is typical and allowed a maximum of 48 radial finite elements. For values of $\beta \lesssim 0.5$ in this sequence this version could not give a reliable estimate of the growth rate and β_c was thus determined by extrapolation from growth rates with β some distance away from the marginal point. For this case one would predict $\beta_c^{(1)} \sim 0.46\%$, about 10% above the value given by PEST 2.

Since, away from marginal stability, calculations such as those given in Section 4.1 show that PEST 1 and PEST 2 agree well, it is reasonable to conclude that the presence of the shear Alfven and slow acoustic mode continua in PEST 1 can make such an extrapolation inaccurate. On the other hand the almost linear behavior of ω^2 against β with PEST 2, even into the stable side, leaves little doubt as to the accuracy of this approach. The absence of any continuum (up to $\omega^2 = |D_I|/\Gamma$) allow ω^2 to be an analytic function of β in the vicinity of $\omega^2 = 0$. In contrast, even if it were practical to follow the unstable ballooning mode into the continuum on the stable side with the approach of PEST 1, it would be almost certain that $d\omega^2/d\beta$ would be discontinuous across $\omega^2 = 0$ [24].

4.3. *Choice of Coordinate System*

For tokamak equilibrium parameters of interest to present experiments and reactor designs, our experience with various choices of Θ does not allow us to make any strong statement about an optimal coordinate system. Even in the case of high-β ballooning modes, the use of a global Fourier expansion in Eq. (52) demands a good representation of the equilibrium in the region near $\Theta = \pi$ because, since $|\xi| \approx 0$ in this region, insufficient numerical accuracy will prevent an accurate minimization of $\mathbf{Q}_\perp^2$ (part of the first term in Eq. (31)) and hence underestimate (or stabilize) the growth rate. The best choice for Θ may, of course, be determined by the requirements for an accurate and efficient calculation of the toroidal equilibrium, or by the need to compute accurately various derivatives of the equilibrium metric. Since these issues are problem dependent, one of the values of allowing for an arbitrary Jacobian lies in the extra confidence in the results which comes from obtaining consistent growth rates from different coordinate systems.

Because it distributes mesh points uniformly over the plasma surfaces, the equal arc Θ ($\mathscr{J} = X/\alpha\,|\nabla\psi|$) is usually a good choice. For a small aspect ratio device like the spheromak [30], where the PEST Θ does not sample the region on the outboard side of the torus very well, an equal arc length system is indeed greatly superior. To

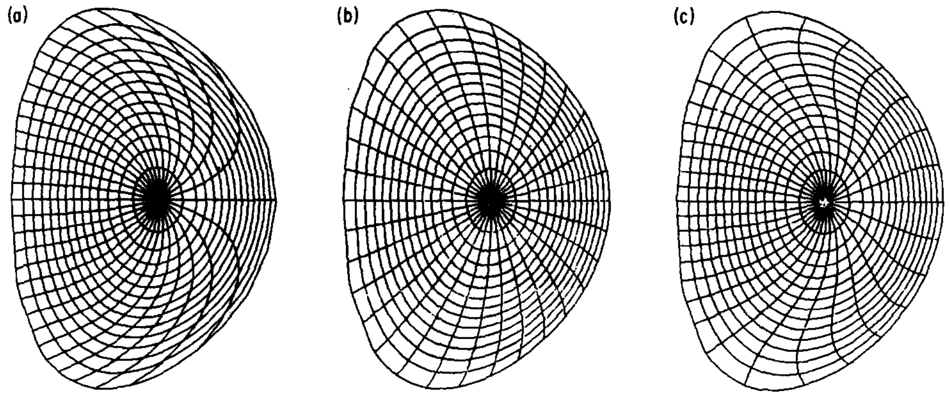

FIG. 5. (a) PEST, (b) equal arc, and (c) $1/B^2$ equally spaced (ψ, Θ) coordinate meshes for a spheromak equilibrium.

illustrate this we compare the convergence of the Fourier representation for four different coordinate systems for an $n = 1$ tilting mode in an equilibrium of the spheromak type. Figures 5a and b show equally spaced (ψ, Θ) meshes for PEST and equal arc length coordinates. From Fig. 6, where we plot the computed growth rate squared versus the number of Fourier modes, we see that these coordinates bracket the convergence rates of the four systems chosen. The equal arc length system is rapidly convergent, with an error of only 0.2% of its final converged value with $-4 \leqslant l \leqslant 4$. Comparable accuracy with PEST coordinates requires approximately three times as many Fourier components. In Fig. 7 we show the radial variation of

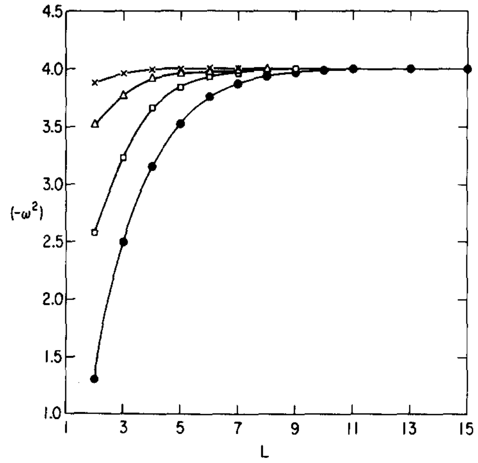

FIG. 6. Convergence of growth rate squared versus number of Fourier components for (●) PEST, (□) Hamada, (△) $1/B^2$, and (×) equal arc length coordinate systems for the spheromak equilibrium of Fig. 5.

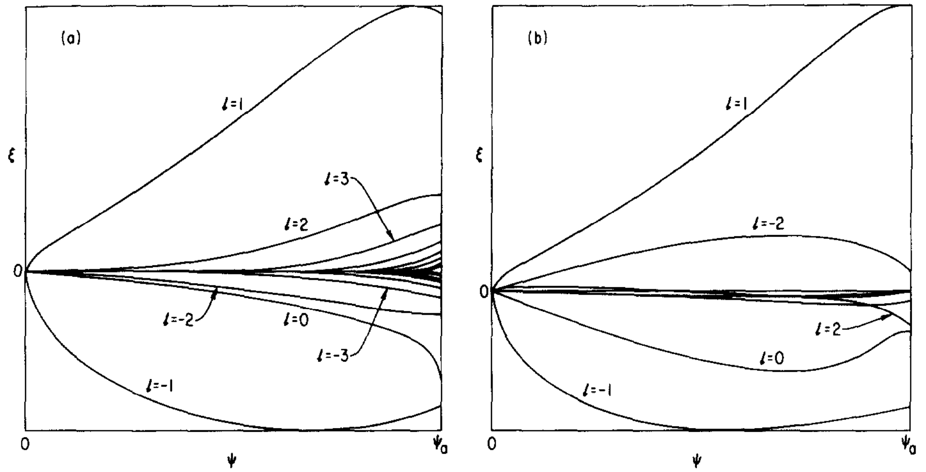

FIG. 7. The ψ-dependence of different Fourier components in the unstable eigenfunction for the $n = 1$ tilting mode using (a) PEST and (b) equal arc length coordinate systems.

the different Fourier modes for these two coordinate systems for the case $L = 10$, $(-10 \leqslant l \leqslant 10)$ illustrating again that the tilting mode is well represented by the equal arc length coordinates system with only a few Fourier modes. The inadequacy of the Θ_p mesh would be more pronounced at smaller aspect ratios.

Results for two additional coordinate systems are shown in Fig. 6. A Hamada coordinate system converges slightly faster than PEST coordinates, but suffers similar problems in accurately representing the outboard side of the spheromak equilibrium. Finally we have briefly studied the system $\mathscr{J} \propto 1/B^2$, because of its usefulness in the representation of three-dimensional equilibrium fields [31]. It can be seen from Fig. 5c that this choice approximates an orthogonal mesh near the plasma edge and PEST coordinates near the magnetic axis where X^2B^2 is nearly constant. In this case, where the minimizing contribution to δW is not concentrated near the separatrix region, the convergence properties are very good.

5. DISCUSSION

In this paper we have described a numerical approach which represents a significant advance in our capability of determining the ideal MHD stability of axisymmetric toroidal confinement systems. The computational demands are significantly reduced from previous approaches, allowing the possibility of studying instabilities with much larger toroidal mode numbers. Improvements in the representation of the displacement vector $\boldsymbol{\xi}$, and the analytic elimination of two of its components give increased accuracy, while the ability to follow an unstable mode across the point of marginal stability greatly enhances our confidence in the determination of critical equilibrium quantities.

In tokamak design optimization, PEST 2 is now used routinely in place of PEST 1, its principal shortcoming being the inability to produce physical growth rates and eigenfunctions. These could be of importance in the direct comparison with experiments, in the design of feedback systems (e.g., for axisymmetric instabilities), and in studies which demand a detailed knowledge of the stable ideal MHD spectrum (e.g., wave heating). In principle, however, the approach of this paper can be generalized to retain the magnetoacoustic branches of the spectrum by repeating the analysis described in the Appendix with the proper kinetic energy normalization. This results in a set of scalar Euler–Lagrange equations (similar to those for the diffuse pinch), whose Galerkin form involves the eigenvalue ω^2 in a transcendental fashion. We hope to report on this approach in the future, solving the nonlinear eigenvalue problem by iteration in ω^2.

Additional work must concentrate on the appropriate representation of $\boldsymbol{\xi} \cdot \nabla\psi$ near the rational surfaces. Although this can be of importance to some marginally unstable ideal MHD modes (e.g., the internal $m = 1$ kink), it is of critical importance to a boundary layer treatment of nonideal instabilities (e.g., the resistive tearing modes). We shall report on this aspect of linear stability theory in the future.

APPENDIX: A SCALAR FORM OF δW

Here we repeat the principal steps followed in deriving the form of δW given in Eq. (39). In summary the procedure involves solving two components of the Euler–Lagrange equation corresponding to Eqs. (29), (31), and (38) to express ξ^s and ξ^b of Eq. (37) in terms of ξ^ψ and $\partial_\psi \xi^\psi$. Substituting these expressions into the $\nabla\psi$ component yields Eq. (39).

The Euler–Lagrange equation is

$$\omega^2 \boldsymbol{\rho} \cdot \boldsymbol{\xi} + \mathbf{F}(\boldsymbol{\xi}) = 0, \tag{A1}$$

with

$$\begin{aligned}\mathbf{F}(\boldsymbol{\xi}) \equiv {} & -\mathbf{B} \times [\nabla \times (\mathbf{Q} + \xi_n \mathbf{J} \times \mathbf{n})] - \mathbf{n}\mathbf{J} \times \mathbf{n} \cdot (\mathbf{Q} + \xi_n \mathbf{J} \times \mathbf{n}) \\ & + 2U\, \nabla\psi(\boldsymbol{\xi} \cdot \nabla\psi) + \nabla(\gamma p \nabla \cdot \boldsymbol{\xi}),\end{aligned} \tag{A2}$$

$n \equiv \nabla\psi/|\nabla\psi|$, and $\xi_n \equiv \boldsymbol{\xi} \cdot \mathbf{n}$. The model density tensor in Eq. (38) has been chosen so that $\mathbf{B} \cdot \boldsymbol{\rho} = \mathbf{B} \times \nabla\psi \cdot \boldsymbol{\rho} = 0$. Thus the $\mathbf{B}$-component of Eq. (A1) is

$$\mathbf{B} \cdot \mathbf{F} = \mathbf{B} \cdot \nabla(\gamma p \nabla \cdot \boldsymbol{\xi}) = 0, \tag{A3}$$

a magnetic differential equation which, when integrated with the appropriate solubility condition, yields

$$\nabla \cdot \boldsymbol{\xi} = \langle \mathscr{T} \boldsymbol{\xi} \cdot \nabla\psi \rangle' / \langle \mathscr{T} \rangle, \tag{A4}$$

leading to the third term of Eq. (39). This term contributes only for axisymmetric ($n = 0$) perturbations.

The other surface component of the Euler–Lagrange equation yields

$$\nabla \cdot [(\mathbf{Q} + \xi_n \mathbf{J} \times \mathbf{n}) \times \nabla\psi] = 0, \tag{A5}$$

from which the remaining surface component of $\boldsymbol{\xi}$ can be eliminated. To do this we write, using Eq. (7),

$$(\mathbf{I} - \mathbf{nn}) \cdot (\mathbf{Q} + \xi_n \mathbf{J} \times \mathbf{n}) = \nabla_s u + \nabla_s v, \tag{A6}$$

where u is periodic in Θ and ζ and v is a many-valued function of position which satisfies

$$\Delta_s v = 0, \tag{A7}$$

and Δ_s is the surface Laplacian operator defined in Eqs. (41) and (44). It is a two-dimensional elliptic operator in the surface variables Θ and ζ, so that Eq. (A7) has a nontrivial solution because the toroidal domain of Δ_s is not simply connected. The v term contributes only when $n = 0$ and leads to $2\delta W'_{\text{ind}}$ of Eq. (39).

To determine u we take the divergence of Eq. (A6) giving (cf. Eq. (40)),

$$\Delta_s u = -\mathcal{T}^{-1} P\xi, \tag{A8}$$

an elliptic equation for u which can be solved using the Green's function operator Δ_s^{-1}. Substituting this solution back into Eq. (A6) we find for all $n \neq 0$,

$$\mathbf{Q} + \xi_n \mathbf{J} \times \mathbf{n} = \nabla\psi(\mathbf{B} \cdot \nabla\xi)/|\nabla\psi|^2 - \nabla_s(\Delta_s^{-1}\mathcal{T}^{-1}P\xi). \tag{A9}$$

These terms lead directly to the first two terms of Eq. (39).

The calculation of the nonperiodic v contribution is more tedious and is similar to the procedure used to determine $n = 0$ inductive contributions to the perturbed vacuum energy when a Green's function technique is employed to minimize δW_{vac} [4]. For an axisymmetric equilibrium we write

$$\nabla_s v = \sum_{j=1}^{2} I_j(\psi)(\mathbf{I} - \mathbf{nn}) \cdot \mathbf{Y}_j, \tag{A10}$$

with

$$\mathbf{Y}_1 = -(1/2\pi)\,\nabla(\zeta + v_1), \qquad \mathbf{Y}_2 = (1/2\pi)\,\nabla(\Theta + v_2), \tag{A11}$$

where $v_1(\psi, \Theta)$ and $v_2(\psi, \Theta)$ are periodic functions of Θ chosen so that

$$\nabla \cdot (\mathbf{I} - \mathbf{nn}) \cdot \mathbf{Y}_j = 0, \qquad j = 1, 2. \tag{A12}$$

It is easily seen that in the coordinate system of Section 2.2, $v_1 = q\delta(\psi, \Theta)$ and v_2 satisfies

$$\partial_\Theta v_2 = (\mathscr{T}\,|\nabla\psi|^2/X^2)\langle\mathscr{T}\,|\nabla\psi|^2/X^2\rangle^{-1} - 1. \tag{A13}$$

Taking the scalar product of Eq. (A6) with $\mathbf{Y}_1$ and $\mathbf{Y}_2$, adding, integrating over the magnetic surface, and using periodicity, we find two equations which determine I_1 and I_2. These are

$$L_j'(\psi)\, I_j(\psi) = V_j'(\psi) \qquad j = 1, 2, \tag{A14}$$

with

$$L_1'(\psi) = \langle\mathscr{T}/X^2\rangle, \qquad L_2'(\psi) = \langle\mathscr{T}\,|\nabla\psi|^2/X^2\rangle^{-1} \tag{A15}$$

and

$$\begin{aligned} V_1'(\psi) &= 2\pi g\langle\mathscr{T}\xi/X^2\rangle, \\ V_2'(\psi) &= -2\pi[\langle\xi'\mathscr{T}\,|\nabla\psi|^2/X^2\rangle + \langle\mathscr{T}\xi(X^2p' + gg')/X^2\rangle \\ &\quad + \langle\mathscr{T}\,\nabla\psi\cdot\nabla\Theta(\partial_\Theta\xi)/X^2\rangle]\langle\mathscr{T}\,|\nabla\psi|^2/X^2\rangle^{-1}. \end{aligned} \tag{A16}$$

With $I_j(\psi)$ determined from Eq. (A14), substitution into Eq. (A10) completes the evaluation of the right-hand side of Eq. (A6) and the additional term can thus be added directly into the right-hand side of Eq. (A9), giving an expression for the first term of Eq. (31) which involves only $\xi = \boldsymbol{\xi}\cdot\nabla\psi$ and its ψ-derivative. These additional $n = 0$ terms are given explicitly in Eq. (45).

Grouped together, the $n = 0$ terms of Eq. (39) give the following contribution to the weak form, Eq. (54):

$$\begin{aligned} W^0_{l'l} &= \gamma p R^*_{0l'} R_{0l}/S_{00} + g^2 N^*_{0l'} N_{0l}/H_{00} + L^*_{0l'} L_{0l}/F^{-1}_{00}, \\ Y^0_{l'l} &= \gamma p S^*_{0l'} R_{0l}/S_{00} + g^2 H^*_{0l'} N_{0l}/H_{00} + F^{-1}_{0l'}{}^* L_{0l}/F^{-1}_{00}, \\ Z^0_{l'l} &= \gamma p S^*_{0l'} S_{0l}/S_{00} + g^2 H^*_{0l'} H_{0l}/H_{00} + F^{-1}_{0l'}{}^* F^{-1}_{0l}/F^{-1}_{00}, \end{aligned} \tag{A17}$$

with

$$\begin{aligned} H_{l'l} &= \langle l'|\,\mathscr{T}/X^2\,|l\rangle, \\ L_{l'l} &= \langle l'|\,[\mathscr{T}(X^2p' + gg') + i(l - l')\mathscr{T}\,\nabla\psi\cdot\nabla\Theta]/X^2\,|l\rangle, \\ N_{l'l} &= \langle l'|\,(\mathscr{T}/X^2)'\,|l\rangle, \\ F^{-1}_{l'l} &= \langle l'|\,\mathscr{T}\,|\nabla\psi|^2/X^2\,|l\rangle, \end{aligned}$$

and $R_{l'l}$, $S_{l'l}$ as given in Eq. (56).

ACKNOWLEDGMENTS

The authors are grateful for many useful discussions with Dr. M. S. Chance and to Dr. J. B. Taylor, who had independently considered the nature of the spectrum of the reduced system studied here. The programming assistance provided by Mr. A. E. Miller was greatly appreciated.

REFERENCES

1. I. B. BERNSTEIN, E. A. FRIEMAN, M. D. KRUSKAL, AND R. M. KULSRUD, *Proc. R. Soc. London, Ser. A* **244** (1958), 17.
2. A. SYKES AND J. A. WESSON, *Nucl. Fusion* **14** (1974), 645.
3. G. BATEMAN, W. SCHNEIDER, AND W. GROSSMAN, *Nucl. Fusion* **14** (1974), 669.
4. R. C. GRIMM, J. M. GREENE, AND J. L. JOHNSON, *Meth. Comput. Phys.* **9** (1976), 253.
5. R. GRUBER, F. TROYON, D. BERGER, L. C. BERNARD, S. ROUSSET, R. SCHREIBER, W. KERNER, W. SCHNEIDER, AND K. V. ROBERTS, *Comput. Phys. Commun.* **21** (1981), 323.
6. R. W. MOORE, L. C. BERNARD, D. DOBROTT, R. L. MILLER, AND F. J. HELTON, *Bull. Amer. Phys. Soc.* **24** (1979), 1044; L. C. BERNARD, F. J. HELTON, AND R. W. MOORE, *Comput. Phys. Commun.* **24** (1981), 377.
7. M. S. CHANCE, J. M. GREENE, R. C. GRIMM, J. L. JOHNSON, J. MANICKAM, W. KERNER, D. BERGER, L. C. BERNARD, R. GRUBER, AND F. J. TROYON, *J. Comput. Phys.* **28** (1978), 1.
8. A. M. M. TODD, M. S. CHANCE, J. M. GREENE, R. C. GRIMM, J. L. JOHNSON, AND J. MANICKAM, *Phys. Rev. Lett.* **38** (1977), 826.
9. D. DOBROTT, D. B. NELSON, J. M. GREENE, A. H. GLASSER, M. S. CHANCE, AND E. A. FRIEMAN, *Phys. Rev. Lett.* **39** (1977), 943.
10. J. W. CONNOR, R. J. HASTIE, AND J. B. TAYLOR, *Proc. R. Soc. London, Ser. A* **365** (1979), 1.
11. R. L. DEWAR, J. MANICKAM, R. C. GRIMM, AND M. S. CHANCE, *Nucl. Fusion* **21** (1981), 493.
12. A. M. M. TODD, J. MANICKAM, M. OKABAYASHI, M. S. CHANCE, R. C. GRIMM, J. M. GREENE, AND J. L. JOHNSON, *Nucl. Fusion* **19** (1979), 743.
13. J. T. HOGAN, *Nucl. Fusion* **19** (1979), 753.
14. S. C. JARDIN, *J. Comput. Phys.* **43** (1981), 31.
15. K. APPERT, D. BERGER, R. GRUBER, AND J. RAPPATZ, *J. Comput. Phys.* **18** (1975), 284.
16. R. GRUBER, S. SEMENZATO, F. TROYON, T. TSUNEMATSU, W. KERNER, P. MERKEL, AND W. SCHNEIDER, *Comput. Phys. Commun.* **24** (1981), 363.
17. W. M. TANG, R. L. DEWAR, AND J. MANICKAM, PPPL-1895; *Nucl. Fusion* **22** (1982), 1079.
18. R. GRUBER, F. TROYON, S. ROUSSET, W. KERNER, AND L. C. BERNARD, *Comput. Phys. Commun.* **22** (1981), 383.
19. J. L. JOHNSON, H. E. DALHED, J. M. GREENE, R. C. GRIMM, Y. Y. HSIEH, S. C. JARDIN, J. MANICKAM, M. OKABAYASHI, R. G. STORER, A. M. M. TODD, D. E. VOSS, AND K. E. WEIMER, *J. Comput. Phys.* **32** (1979), 212.
20. J. M. GREENE AND J. L. JOHNSON, *Phys. Fluids* **5** (1962), 510.
21. L. S. SOLOV'EV, *Zh. Eksp. Teor. Fiz.* **53** (1967), 626; *Sov. Phys.-JETP* **26** (1968), 400.
22. M. BINEAU, *Nucl. Fusion* **2** (1962), 130.
23. K. APPERT, R. GRUBER, AND J. VACLAVIC, *Phys. Fluids* **17** (1974), 1471.
24. M. S. CHANCE, J. M. GREENE, R. C. GRIMM, AND J. L. JOHNSON, *Nucl. Fusion* **17** (1977), 65.
25. A. H. GLASER, J. M. GREENE, AND J. L. JOHNSON, *Phys. Fluids* **18** (1975), 875.
26. I. M. GELFAND AND G. E. SHILOV, "Generalized Functions," Vol. 1, Academic Press, New York, 1964.
27. G. STRANG AND G. J. FIX, "An Analysis of the Finite Element Method," Prentice-Hall, Englewood Cliffs, N.J., 1973.

28. J. Manickam, R. C. Grimm, and R. L. Dewar, *Comput. Phys. Commun.* **24** (1981), 355.
29. R. Gruber, *Comput. Phys. Commun.* **20** (1980), 421.
30. S. C. Jardin, M. S. Chance, R. L. Dewar, R. C. Grimm, J. Manickam, and D. A. Monticello, *Nucl. Fusion* **21** (1981), 1203.
31. A. H. Boozer, *Phys. Fluids* **24** (1981), 1999.